ORIGINAL ARTICLE

Impact of temperature stabilization on the strapdown airborne gravimetry: a case study in Central Turkey

Mehmet Simav[1] · David Becker[2] · Hasan Yildiz[1] · Matthias Hoss[3]

Abstract

Airborne gravimetry with strapdown inertial sensors has been a valuable tool for many years to fill in the gravity data gaps on the areas not accessible by land. Accuracies of 1 mGal level with off-the-shelf navigation-grade inertial measurement units (IMU) can only be achieved provided that the accelerometer drifts mainly caused by the temperature variations inside the IMU housing are separated from the gravity signal. Although there are several strategies proposed in the literature to deal with this inseparability problem, we use a thermal stabilization system (iTempStab) added on an iNAT-RQH navigation-grade IMU and investigate its performance over a test region in central Turkey with moderate topography and highly qualified ground truth gravity data. Two test flights were performed in 2017 and 2018 with and without iTempStab add-on following almost the same flight trajectories. During the first flight in 2017 with iNAT-RQH only, which lasted almost 5.5 h, there were considerable temperature variations inside the IMU housing from 39.1 to 46.0 °C. A simple thermal correction based on a laboratory calibration done before the flight was applied to the vertical Z-accelerometer in the pre-processing stage. However, temperature changes were within 0.1 °C during the second test flight in 2018 with TempStab add-on. The temperature stabilization gained by the iTempStab add-on produced better cross-over statistics. While the RMSE of the non-adjusted cross-over residuals was about 2.6 mGal, it reduced by 50% with iTempStab add-on. The adjusted cross-over differences of the 2018 flight yielded an RMSE of about 0.5 mGal, which is a remarkable precision for the strapdown gravimetry. The comparison with upward continued ground gravity data at flight altitudes suggests that the thermal stabilization system shows also remarkable improvements in the residual statistics. The range of the residuals decreases from ±10 to ±5 mGal, the standard deviation decreases from 2.19 to 0.94 mGal, and the RMSE decreases from 2.24 to 1.48 mGal, respectively, with the iTempStab add-on. It can be concluded that the thermal stabilization system significantly improves the accelerometer stability and therefore the precision and accuracy of the strapdown airborne gravity estimates.

Keywords Strapdown airborne gravimetry · Thermal correction · Thermal stabilization · Extended Kalman filter

1 Introduction

Having a comparable or even better performance in the higher frequency domain than traditional stable-platform gravimeters, strapdown inertial measurement units (SIMUs) have been used as airborne gravimetry sensors since the early 1990s. (Schwarz et al. 1992; Jekeli 1994; Wei and Schwarz 1998; Glennie et al. 2000; Bruton et al. 2002; Deurloo 2011; Ayres-Sampaio et al. 2015; Becker et al. 2015; Jensen and Forsberg 2018). Besides being smaller in size and cheaper in price, and having lower energy consumption, and ease of operation compared to platform-stabilized airborne gravimeters, SIMU has the potential to determine the full 3-D gravity vector. However, the uncompensated long-term drift effect of the off-the-shelf SIMU accelerometers on the gravity estimations is the main disadvantage of the strapdown gravimetry. A considerable portion of the accelerometer drifts, which may leak into the long wavelengths of the gravity estimates, is caused by the temperature variations in the SIMU housing. Since the accelerometer drifts are almost inseparable from along-track variations of the gravity signal during a non-accelerated horizontal flights, as it is typically the case for

✉ Mehmet Simav
  mehmet.simav@harita.gov.tr

[1] Geodesy Department, General Directorate of Mapping, Ankara, Turkey

[2] Physical and Satellite Geodesy, Technische Universität Darmstadt, Darmstadt, Germany

[3] iMAR Navigation GmbH, St. Ingbert, Germany

airborne campaigns, neither the accelerometer errors nor the gravity signal is directly observable but only the combination can be detected (Glennie and Schwarz 1999; Jekeli and Kwon 1999; Glennie et al. 2000; Becker 2016). There exist different strategies in the literature to deal with this inseparability problem (Glennie and Schwarz 1999; Hwang et al. 2006; Deurloo 2011; Ayres-Sampaio et al. 2015), such as flight maneuvers (e.g., rotations around the roll or pitch-axes), removal of linear drifts for individual flight lines using redundant or external measurements (e.g., cross-over residuals, global gravity models), each have their pros and cons. Becker et al. (2015) and Becker (2016) suggest using IMU calibration methods without applying any bias or drift removal to the gravity estimates to achieve accuracies of 1 mGal level. As an alternative to thermal calibrations and corrections applied to the accelerometers, Becker (2016) also recommends using SIMU with an internal thermal stabilization system or a thermally insulated housing for the SIMU.

Within the Turkish Height System Modernization and Gravity Recovery Project which aims to develop a high-quality geoid model for Turkey (Simav and Yildiz 2019), the General Directorate of Mapping ordered an iNAT navigation-grade SIMU from iMAR company (https://www.imar-navigation.de/en/) in 2016 to perform airborne surveys above the remote areas not accessible by land. Soon after the first test flight (F-2017) performed in 2017 in Turkey, the iNAT was upgraded with an add-on temperature stabilization system called iTempStab. In 2018, one more test flight (F-2018) was conducted by iNAT with iTempStab add-on using the same aircraft and following almost the same flight trajectory of F-2017. This study focuses on the performance of iTempStab add-on by analyzing the airborne gravimetry campaign data of two test flights in central Turkey. Results from the F-2017 obtained without iTempStab add-on, but Z accelerometer measurements corrected for the thermal effect is compared to F-2018 flight acquired with iTempStab add-on. A recent study by Jensen et al. (2019) also evaluated the performance of iTempStab over the Kattegat Sea between Denmark and Sweden by operating temperature stabilized SIMU alongside a traditional spring-type platform-stabilized gravity system. They compared the gravity estimates from both systems and concluded that iTempStab add-on effectively limits the accelerometer drift and improves the long-wavelength gravity field information.

The second and third parts of the manuscript are devoted to SIMU and GNSS data acquisition and the processing methodology that is the integration of SIMU and GNSS observations using a Kalman filter. Section four compares the results and evaluates the performance of iTempStab add-on. The manuscript is concluded with a summary of the central findings.

## 2 Instrumentation and campaign overview

One of the most challenging objectives of the Turkish Height System Modernization and Gravity Recovery Project is the airborne gravimetry which aims to fill in the gravity data gaps on the areas not accessible by land, e.g., lakes, coastal zones, and mountainous regions to determine a high precision and resolution geoid model for Turkey. For this purpose, the General Directorate of Mapping purchased a navigation-grade iNAT-RQH-1001 unit from iMAR Navigation GmbH, which consists of servo accelerometers triad of type QA2000-030, three high precision and airborne proven GG1320AN ring laser gyroscopes, a temperature sensor, an integrated NovAtel GNSS receiver, and a PC board. The PC board gathers information from the sensors and GNSS receiver and then provides time-stamped inertial raw data (turn rates and accelerations) along with the temperature. It has also the ability to output the real-time navigation solution as well as the sensor error estimations using its internal online 27+ states Kalman filter software.

The first flight of the airborne gravimetry test campaign was carried out with iNAT-RQH-1001 unit only on March 22, 2017, over a test region located east of Ankara in central Turkey with moderate topography varying from 500 to 1500 m and with highly qualified and relatively dense ground truth gravity data with a range of about 350 mGal. A grid type of survey consisting of six north–south and three east–west flight lines each spaced roughly 20 km apart were flown at nearly a constant altitude of 3055 m above sea level and an average ground speed of 80 m/s. The lengths of each north—south and east–west lines were about 120 km and 110 km, respectively.

iNAT-RQH-1001 was upgraded with an iTempStab temperature stabilization system add-on by the manufacturer shortly after the first flight test. The iTempStab add-on contains an integrated TEC (Peltier based heater/cooler) and thermal insulation to allow temperature stabilization of the iNAT system to a precision better than 0.1 K after a few hours of the warm-up period. Immediately after power cycling, iTempStab add-on checks the environmental temperature (t_E) and sets the reference temperature (t_R) to $t_E + 20$ K and rounds it to the next integer value. This is the approximate value that is generated due to the self-heating effect inside of the isolated housing and guarantees a very quick operation at the perfect thermal working point. Assuming a stable environmental temperature, it leads to the situation that the iTempStab needs neither heating nor cooling power at the operation point. It only has to compensate for the external changes of temperature with a proportional consumption of power. Any change in t_E simply changes the power consumption of iTempStab add-on and guarantees accurate stabilization for $t_{E(initial)} \pm 15$ K. For t_E above 45 °C the fans on the iTempStab add-on starts working. The max-

Fig. 1 **a** iNAT-RQH-1001 itself, **b** top view of iNAT-RQH-1001 with iTempStab add-on, **c** back view of iNAT-RQH-1001 with iTempStab add-on, **d** front view of iNAT-RQH-1001 with iTempStab add-on

(a)

(b)

(c)

(d)
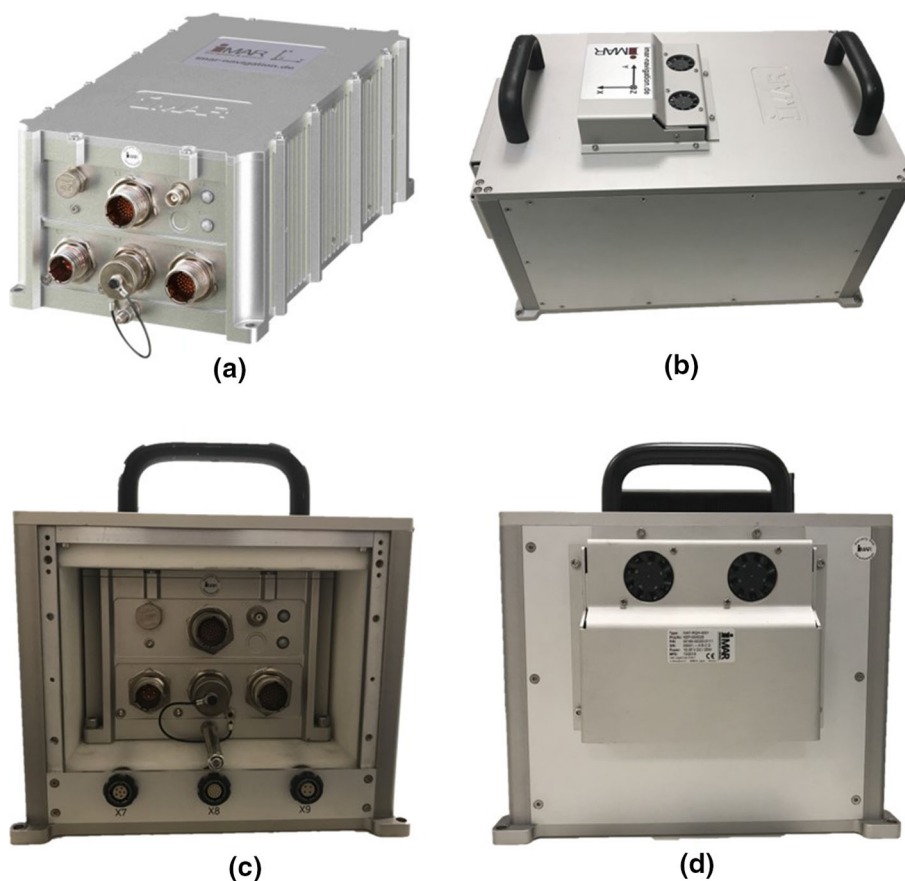
imum control temperature is limited to 55 °C. This method allows the system always to need minimized power consumption during operation. As long as the environmental temperature stays around 27 °C, iTempStab will consume less than 10 W to stabilize the iNAT enclosure temperature to 47 °C. The whole system consumes approximately 35 W then. In maximum cooling, the system consumes up to 150 W. The SIMU and iTempStab add-on used in the study can be seen in Fig. 1 from different perspectives.

The second flight was conducted on September 27, 2018, by iNAT + iTempStab add-on following almost the same flight trajectory and the average velocity of the F-2017 using the aircraft's autopilot. The F-2018 was flown at a little bit higher altitude of about 3180 m than F-2017, and the last two north-south lines (L5 and L6) were interrupted in the middle course due to the logistics. The general flight characteristics are presented in Table 1. Figure 2 shows the trajectories, altitudes and speeds of both flights. Figure 2 also shows the temperature variations inside the physical sensor box called inertial sensor assembly (ISA). It can easily be seen from the figure that while the in-flight ISA temperature of the iNAT changes gradually from 39.1 to 46.0 °C, there is almost no change in the ISA temperature of the iNAT + iTempStab which ranges from 51.9 to 52.0 °C.

Table 1 Flight characteristics

	Flight-2017 (F-2017)	Flight-2018 (F-2018)
Date	22 March 2017	27 September 2018
Flight duration (h)	5.4	5.1
Total length (km)	1545	1421
Avg. altitude above sea level (m)	3055	3180
Avg. flight speed (m/s)	80	80
ISA temperature range (°C)	39.1–46.0	51.9–52.0

During the airborne gravimetry test campaign, iNAT was mounted inside the Beechcraft King Air 200 with the X-axis pointing front, Y-axis pointing right-wing, and Z-axis pointing down directions, and switched on at least 3 h before each take-off to warm up the SIMU for optimal temperature stabilization. The lever arm vector between the SIMU and GNSS antenna was precisely measured by tachymetry. Gravity tie point in front of the hangar was marked with a brass disk and measured using a Scintrex CG-5 relative gravimeter with high precision.
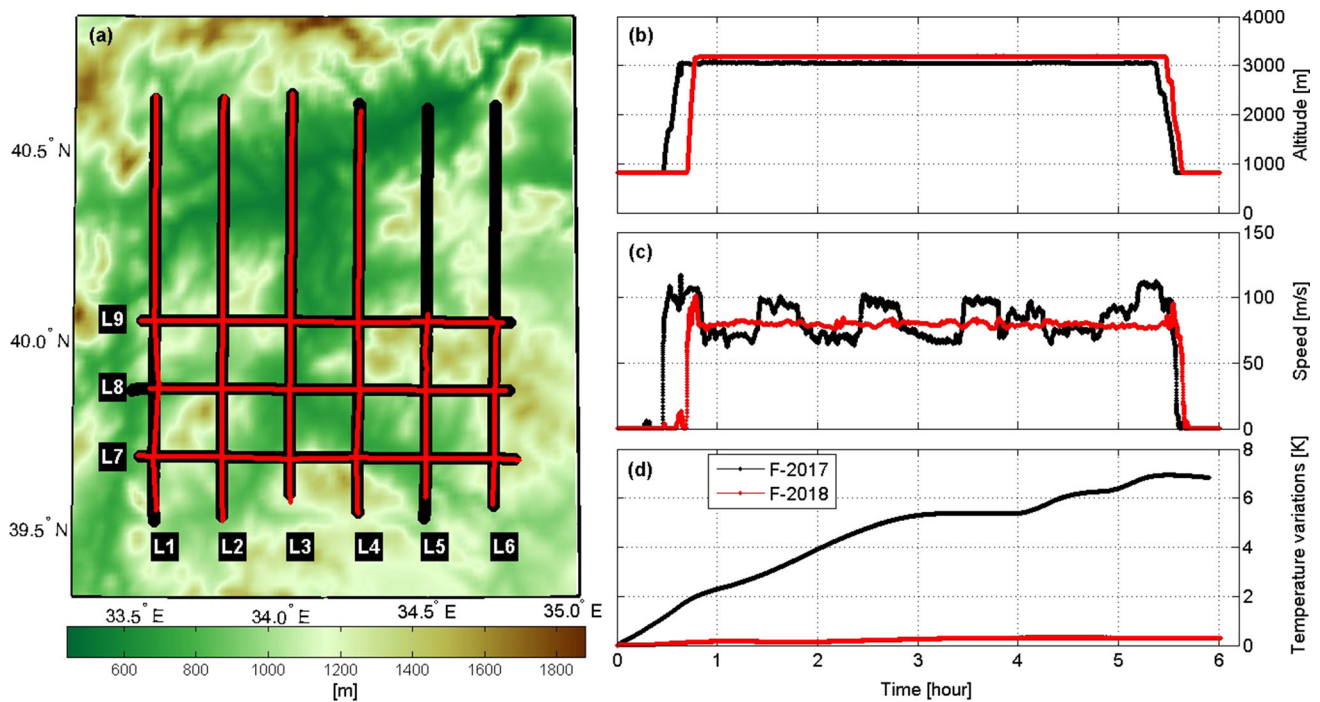
Fig. 2 **a** Horizontal flight trajectories with the line numbers depicted on topography (black: F-2017, red: F-2018), **b** flight altitudes, **c** flight speeds, **d** ISA temperature variations

3 Data and methodology

3.1 SIMU and GNSS data

The strapdown inertial raw acceleration and rotation rate data were collected at 300 Hz. The data message contains the calibrated measurements which include the turn-on sensor errors. The ISA temperature was logged at 1 Hz to model the residual thermal effect. A simple thermal calibration, well described in Becker et al. (2015), Becker (2016) and Jensen (2018), was therefore applied to the vertical Z-accelerometer, based on a laboratory calibration done in March 2017 at the iMAR facilities. The correction, which is a function of ISA temperature and shown in Fig. 3, was applied with a negative sign to the Z-accelerometer measurements of the F-2017.

Data logging was initiated as soon as the aircraft was towed and placed on the gravity tie point at the apron, and at least 10-min-long standstill data was collected to make static alignment and to get initial state estimates.

The rover GNSS receiver integrated to iNAT collected GPS and GLONASS observations at a 1 Hz rate. Because we used loosely coupled IMU/GNSS integration architecture (see Sect. 3.2), GNSS position and velocity solutions were first produced using NovAtel's Waypoint GrafNav 8.80 software before the integration. We applied precise point positioning (PPP) method using the Center for Orbit Determination in Europe (CODE) final GNSS orbit and clock products to get the position and velocity estimates as well as their associated error covariance matrices.

3.2 SIMU/GNSS integration

The integration of SIMU raw data and GNSS solution was achieved by 18 states loosely coupled Extended Kalman Filter (EKF) in the navigation frame (North-East-Down or n-frame). For numerical stability, the integration architecture comprised error-state formulation and closed-loop correction implementation (Groves 2013).

While the gravity disturbance can be computed directly by subtracting the SIMU sensed accelerations from GNSS-derived kinematic accelerations given in the same coordinate frame and applying a low-pass filter to the difference (Glennie and Schwarz 1999; Glennie et al. 2000; Forsberg et al. 2001; Hwang et al. 2006; Forsberg and Olesen 2010; Sampietro et al. 2017), here we used indirect or one-step approach, which includes the vertical gravity disturbance in the system states and model the inertial sensor errors and gravity disturbance as stochastic processes (Schwarz and Wei 1990; Kwon and Jekeli 2001; Tomé 2002; Deurloo 2011; Deurloo et al. 2015; Becker et al. 2015; Ayres-Sampaio et al. 2015). Since the gravity disturbance is the difference between the actual and normal gravity produced by the reference ellipsoid (Heiskanen and Moritz 1967), numerical values of the GRS80 reference ellipsoid and the closed formula given in
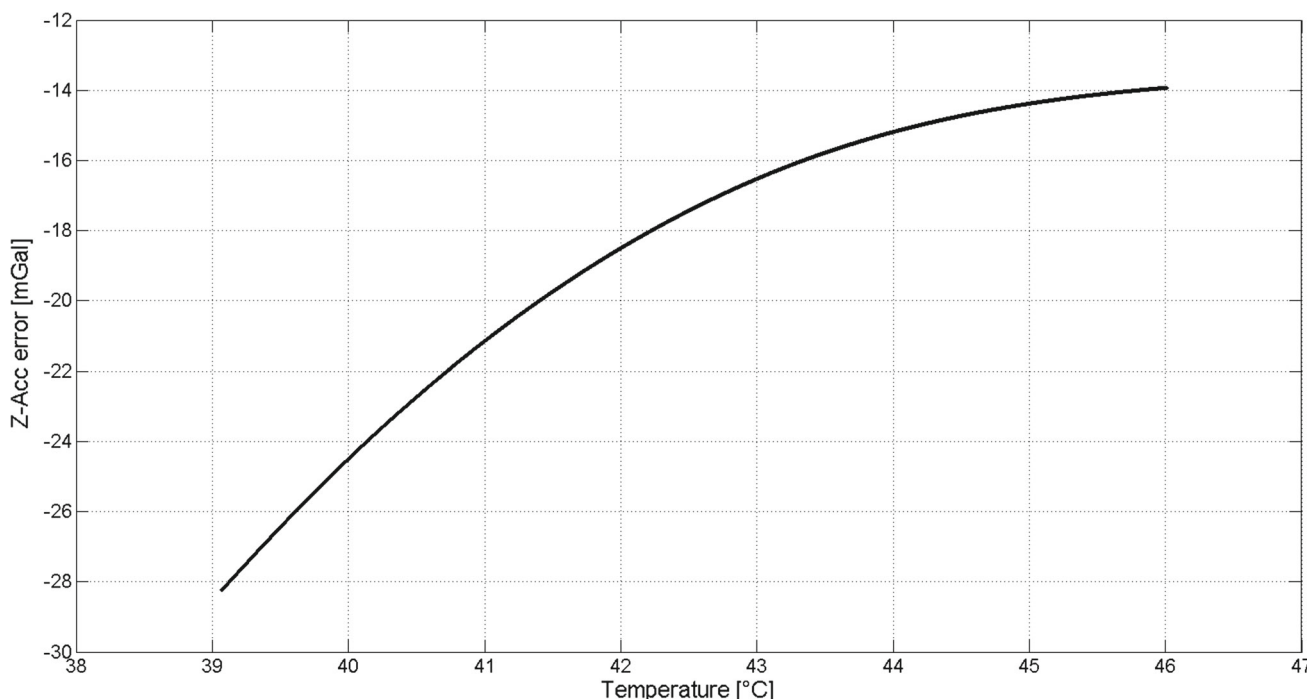
Fig. 3 Z-accelerometer errors in dependence of the ISA temperature obtained from laboratory calibration done in March 2017 at the iMAR facilities

Moritz (2000) were used for the computation of the normal gravity.

While the accelerometers and gyroscopes biases were modeled by a simple random walk model with a system noise, the gravity disturbance was modeled as a third-order Gauss—Markov process (Jekeli 1994; Becker et al. 2015; Jensen and Forsberg 2018), which can be characterized by the below-given autocorrelation function $R(\tau)$ (Gelb 1974):

$$R(\tau) = \sigma^2 e^{-\beta|\tau|}\left(1 + \beta|\tau| + \frac{1}{3}\beta^2|\tau|^2\right) \quad (1)$$

where σ and β represent the standard deviation and the correlation parameter, respectively. The gravity correlation parameter usually expressed in the distance unit is the inverse of the correlation time which should be given in units of time. The conversion between distance and time units could be done during the data processing using the current horizontal flight speed (v_{hor}) as follows (Deurloo 2011):

$$\beta[\text{time}] = v_{\text{hor}}\beta[\text{dist}] = \sqrt{v_N^2 + v_E^2}\,\beta[\text{dist}] \quad (2)$$

Given a typical horizontal flight speed of 80 m/s and β[dist] of 1/20 km^{-1}, the conversion results in β[time] of 0.004 sn^{-1}.

The system's error-state vector $\delta\boldsymbol{x}$ at any time epoch contains the 3-D errors in position ($\delta\boldsymbol{p}^n$), velocity ($\delta\boldsymbol{v}^n$) and attitude ($\delta\boldsymbol{\psi}^n$) in the navigation frame, 3-D accelerometer bias ($\delta\boldsymbol{b}_a^b$) and gyroscope bias ($\delta\boldsymbol{b}_g^b$) in the body frame and

the 1-D vertical gravity disturbance ($\delta\Delta g_D^n$), and it's first ($\delta\Delta\dot{g}_D^n$) and second derivatives ($\delta\Delta\ddot{g}_D^n$) in the navigation frame as follows:

$$\delta\boldsymbol{x} = \left[\, \delta\boldsymbol{p}^n \ \delta\boldsymbol{v}^n \ \delta\boldsymbol{\psi}^n \ \delta\boldsymbol{b}_a^b \ \delta\boldsymbol{b}_g^b \ \delta\Delta g_D^n \ \delta\Delta\dot{g}_D^n \ \delta\Delta\ddot{g}_D^n \,\right]^{\mathrm{T}} \quad (3)$$

GNSS position and velocity solutions were used as measurements in the EKF taking the lever arm vector into account. Moreover, the gravity tie observations and the zero velocities at the aircraft's parking positions were also introduced as measurements to the EKF. The forward EKF estimates were then smoothed using the Rauch–Tung–Striebel (RTS) smoother (Rauch et al. 1965).

4 Analysis and results

The data processing was performed by the Strapdown Airborne Gravimetry (SAG) Processing Software v.1.0. developed by the General Directorate of Mapping in the MATLAB environment. The EKF part of the software is implemented in MEX/C to speed up the calculations. It takes less than 1-min single-core computation time to process the 6-h flight data. It has the capability of performing parallel computations using multicore processors for multiple flight sets and has a user-friendly graphical interface to facilitate the user inputs and settings. There are also post-processing, visualization and export tools in the software such as auto and manual

straight flight line detection, cross-over detection and adjustment, autocorrelation analysis, 2D–3D line plots, contour and surface plots, geographic plots, and data or solution exports in user-selected formats.

The processing algorithm starts with the initialization procedure and is based on two main steps: prediction and measurement update. While the SIMU position is initialized with GNSS solution, attitude is initialized through leveling and gyrocompassing (Groves 2013), and vertical gravity disturbance is initialized with local gravity tie available at the aircraft's parking position. The remaining states, velocity and sensor biases, are initialized with zero. Initial uncertainties for the states' error covariance matrix and the system noises of the state variables used in the processing are presented in Table 2.

After the initialization, inertial navigation (Groves 2013) is performed to update the current estimates of position, velocity and attitude until the next measurement is available by sequentially adding small increments derived by integrating the SIMU-specific force and angular rate observations. The attitude update is based on quaternions rather than the direction-cosine matrix representation. The estimates of the sensor biases and the gravity disturbance remain unchanged in the prediction step if a simple random walk model is used or change due to derivatives when higher-order Gauss–Markov is used. During the prediction step, the error covariance matrix is also propagated forward in time at a user-defined update rate based on previous error covariance, state transition and system noise covariance matrices. When any GNSS position and velocity or terrestrial gravity or zero velocity measurements are available, the filtering is applied immediately. In this stage, standard EKF formulas are used to estimate the state's errors and to update the error covariance matrix using measurement matrix, measurement noise covariance matrix, Kalman gain matrix, measurement innovation vector and predicted error covariance matrix. After each measurement update, the estimated error-state vector is applied to the system states and is zeroed at once. Finally, the integrated SIMU/GNSS solution was smoothed using RTS smoother implementation.

Table 2 EKF settings used in the processing

Error state	Initial uncertainty	System noise
Position	2 cm	0 m/$\sqrt{s}$
Velocity	10 cm/s	5E−5 m/s/$\sqrt{s}$
Attitude [roll, pitch, yaw]	[1, 1, 5]°	0.2 arcsec/$\sqrt{s}$
Accelerometer bias	100 mGal	0.01 mGal/$\sqrt{s}$
Gyroscope bias	0.001 °/h	0 °/h/$\sqrt{s}$
Vertical gravity disturbance	0.03 mGal	$\sigma_{dg} = 100$ mGal $\beta_{dg}^{3rd} = 1/20$ km^{-1}

The final gravity disturbance solutions were acquired iteratively. After the first iteration, the autocorrelation function $R(\tau)$ was computed as a function of along-track distance for each flight line. Then the third-order Gauss-Markov model given in Eq. (1) was fitted to the $R(\tau)$ in a least squares manner to estimate σ and β parameters. Figure 4 shows the autocorrelation function of each flight line in black and the best fit in red. The nonlinear least squares fit yielded parameters of $\sigma = 16.87$ mGal and $1/\beta = 3.27$ km, which were subsequently used in the second processing iteration. The final vertical gravity disturbance estimates for the two test flights are shown in Fig. 5. The strong correlation between the gravity and topography variations can easily be seen from the figures.

4.1 Cross-over evaluation

The internal precision of the gravity disturbance estimates from both flights was assessed at the cross-over points where two individual flight lines are intersecting horizontally. It is obvious that the tree-dimensional flight paths are hardly repeatable and seldom intersect at the same point due to the changing conditions. In practice, altitude differences reaching up to a few hundred meters can be observed at the cross-over locations. Therefore, special care must be given when selecting a cross-over point because of the height-dependent gravity variations. But, by limiting the height differences as small as possible (e.g., $\Delta H_{\max} < 100$ m), the majority of free-air gravity gradient effect will be accounted for by the normal gravity gradient when comparing gravity disturbances. Assuming negligible time-dependent variations in the gravity field due to the tides, groundwater and air pressure changes, ocean loading, nutation and precession, the cross-over difference between two flight trajectories can be expressed as:

$$\chi_{A,B} = \delta\widehat{g}_A - \delta\widehat{g}_B \tag{4}$$

$$\overline{\chi}_{A,B} = \left(\delta\widehat{g}_{A_i} + \kappa_A\right) - \left(\delta\widehat{g}_{B_j} + \kappa_B\right) \tag{5}$$

If there is a sufficient number of cross-over data, a least squares adjustment can be performed and a shift parameter κ can be computed for each flight line. Given $\delta\widehat{g}_{A_i}$ and $\delta\widehat{g}_{B_j}$ as the i-th and j-th cross-over points on lines A and B, respectively, the adjusted cross-over residuals $\overline{\chi}_{A,B}$ can be written as Eq. (5).

Figure 6 shows the 18 cross-over point locations and the adjusted gravity disturbance differences for both flights. The root-mean-squared errors (RMSE) of the non-adjusted and adjusted cross-over differences are also presented in Table 3. While the simple thermal correction yielded a significant reduction in the non-adjusted RMSE of the F-2017 flight, ISA temperature stabilization with iTempStab experienced
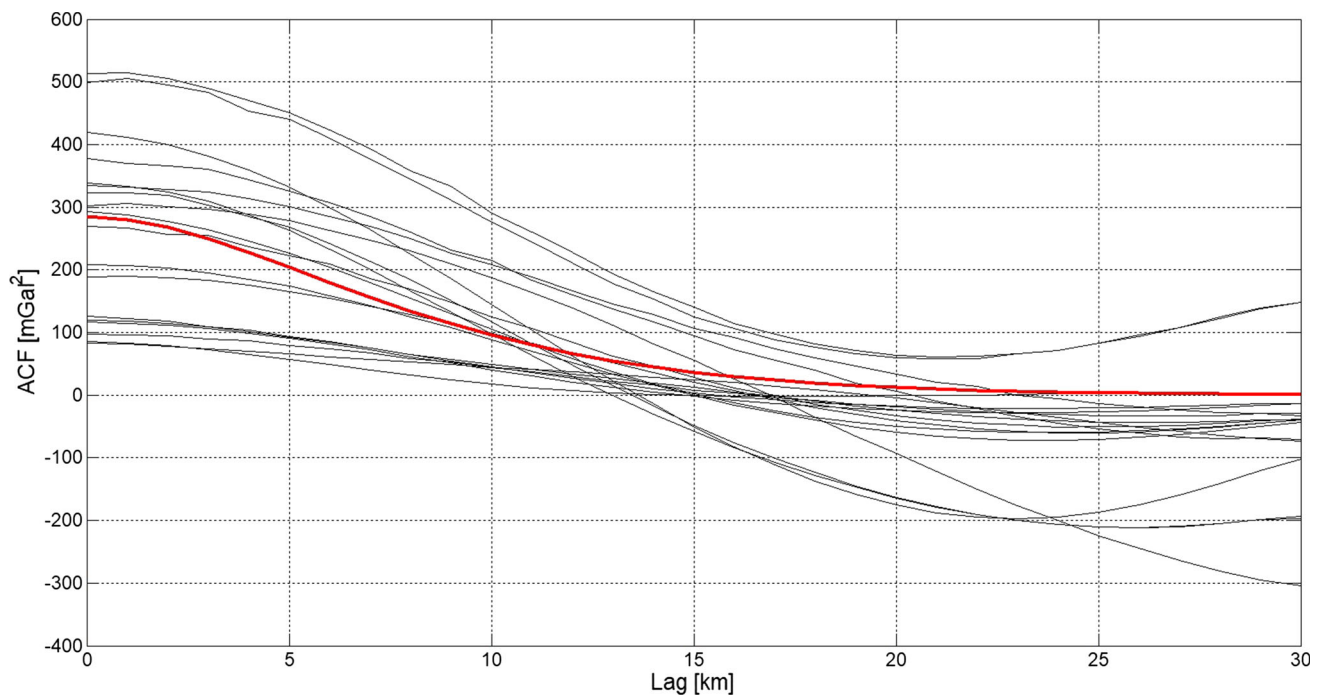
Fig. 4 Autocorrelation functions (ACFs) for the nine F-2017 and nine F-2018 profiles in black along with the best fitting third-order Gauss–Markov autocorrelation function in red
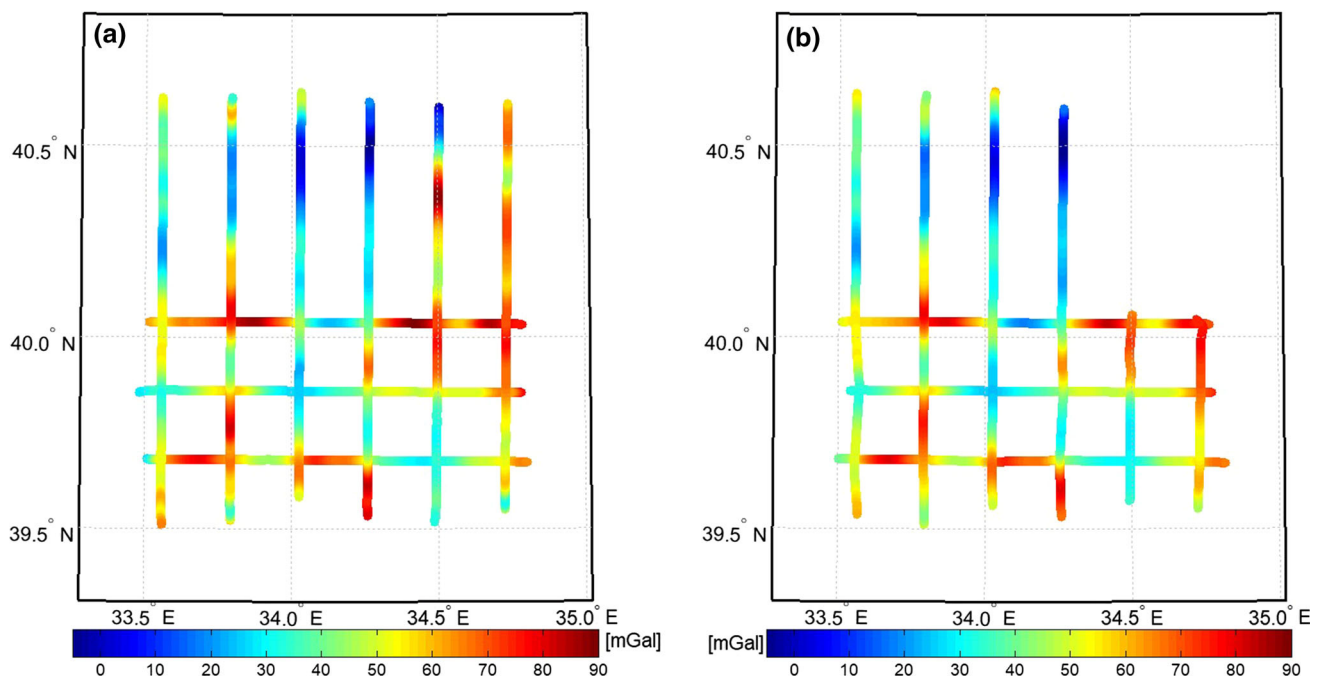

Fig. 5 Vertical component of the estimated gravity disturbance along the straight line segments. **a** F-2017, **b** F-2018

in the F-2018 test flight produced better results. The RMSE reduced by 50% from 2.6 to 1.3 mGal with the contribution of iTempStab. The mean of the non-adjusted cross-over differences of F-2018 is close to zero which suggests that the constant bias due to the thermally driven accelerometer drift is compensated by temperature stabilization.

As expected, the cross-over adjustment improved the statistics drastically. Applying an adjustment to the network of cross-overs leads to significantly smaller residuals. It can be concluded that the majority of the non-adjusted residuals aroused from constant offsets, as they are known to appear in particular due to thermal effects. Although
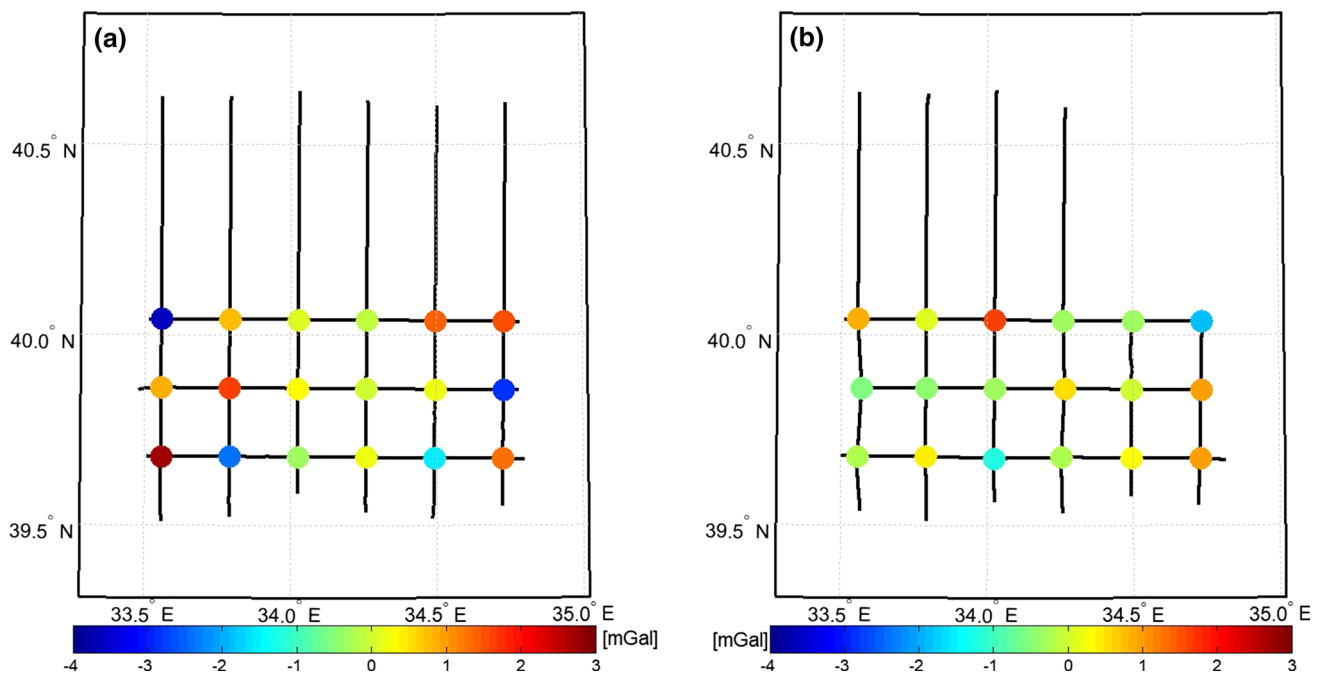
Fig. 6 Vertical gravity disturbance differences at 18 cross-over points after the cross-over adjustment. **a** F-2017, **b** F-2018

Table 3 Cross-over statistics

	Non-adjusted (mGal)			Adjusted (mGal)		
	μ	σ	RMSE	μ	σ	RMSE
F-2017 without TC	− 4.39	3.14	3.78	0.00	1.79	1.23
F-2017 with simple TC	− 1.85	3.20	2.56	0.00	1.67	1.14
F-2018 with iTempStab	− 0.02	1.88	1.29	0.00	0.83	0.57

TC temperature correction, μ mean, σ standard deviation, RMSE: RMS/$\sqrt{2}$

the Z-accelerometer was corrected using a simple thermal correction, some residual long-term drifts still appeared to remain in the F-2017 data. The adjusted cross-over residuals of the F-2018 flight have RMSE of 0.6 mGal, which is a promising and remarkable precision for the strapdown gravimetry. It should be noted here that, since the maneuvers such as turns are expected to lead to slight decreases in precision, we could obtain as low as 0.4 mGal RMSE when the cross-over points that were closest to the turns of the aircraft were not taken into consideration.

4.2 Upward continuation of ground data

For the external quality assessment or the accuracy determination of the airborne gravity estimates, it is a common practice to compare the upward continued terrestrial gravity values with airborne gravity data at the flight altitude,
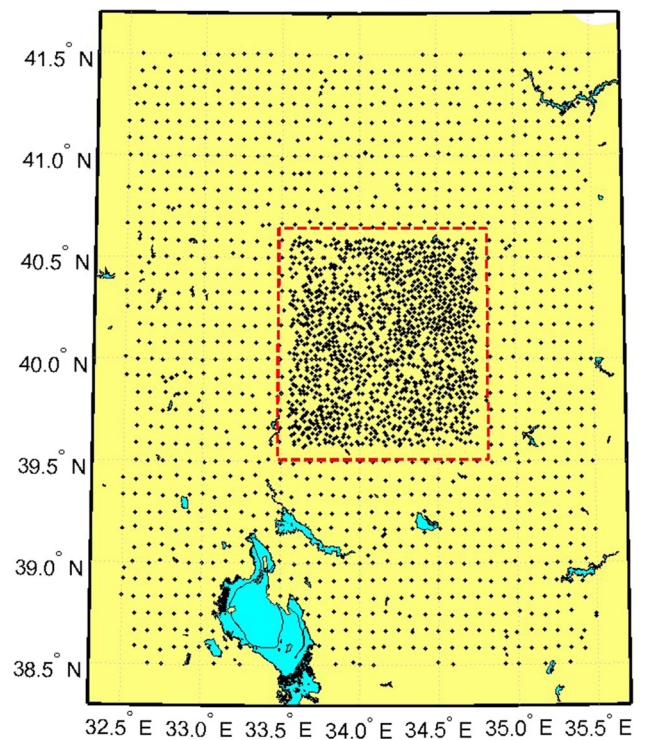

Fig. 7 Distribution of the terrestrial gravity data used in the upward continuation. The red box shows the test region

provided that there are sufficiently dense ground data in and outside the region. Through the height system modernization project, country-wide absolute and relative gravity
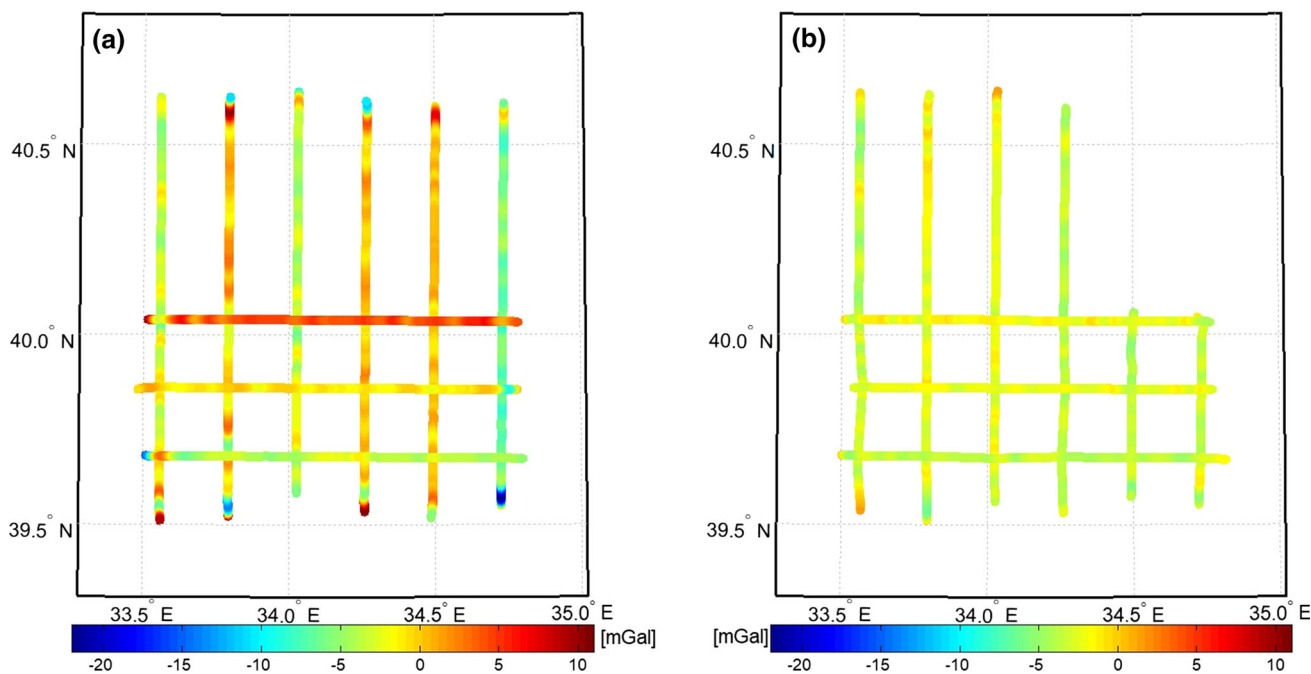
Fig. 8 Vertical gravity disturbance differences between the cross-over adjusted line segments and the upward continued gravity data. **a** F-2017, **b** F-2018
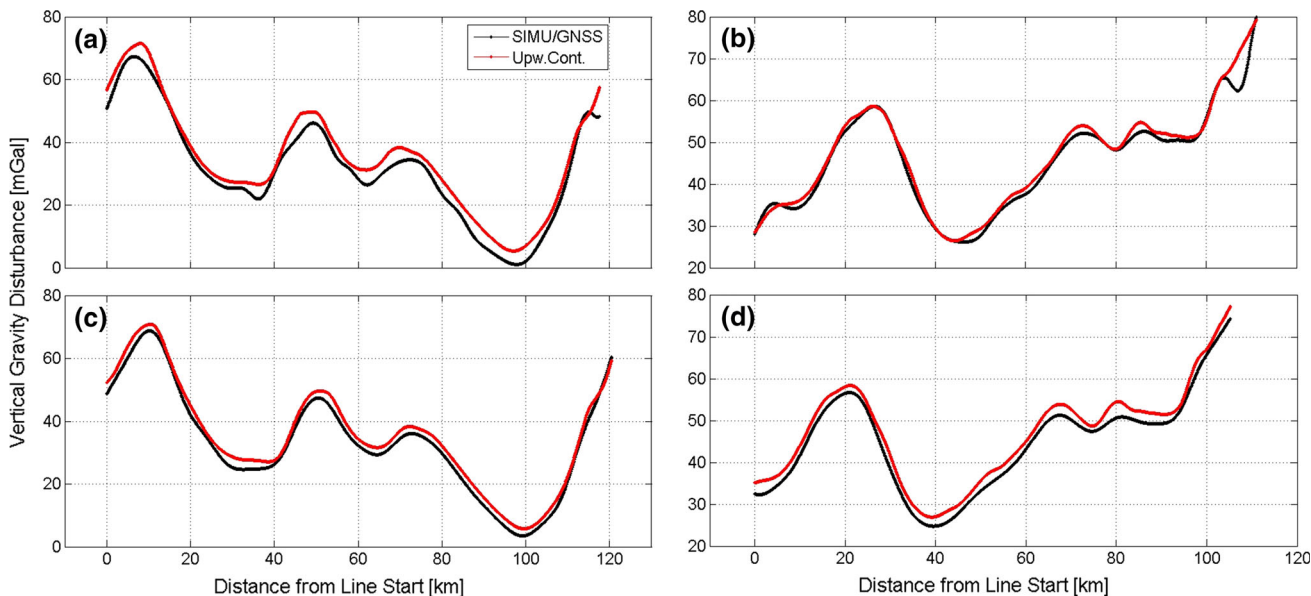

Fig. 9 Comparison of the cross-over adjusted vertical gravity disturbances in black at two different line segments with the upward continued terrestrial data in red. **a** F-2017/Line-3, **b** F-2017/Line-8, **c** F-2018/Line-3, **d** F-2018/Line-8

surveys have been carried out since 2016 to renew the gravity standardization network and to make densification in some specific regions (Simav and Yildiz 2019). The airborne gravimetry test region was measured in 2018 with 2–3 km point spacing inside the test area and 9–10 km outside. Figure 7 shows the distribution of the ground truth data used for the computation of upward continued gravity disturbances at flight altitudes. Simav and Yildiz (2019) explain the absolute

and relative gravity data acquisition and processing in detail. The adjustment of the gravity observations in the test region reduced for environmental and instrumental effects resulted in a mean formal error of 19 μGal.

Multi-processing least squares collocation (Kaas et al. 2013) in remove-upward continue-restore fashion was applied for the computation of upward continued gravity disturbances at flight altitude. Firstly, the GOCO06S

Table 4 Statistics of the vertical gravity disturbance differences between the upward continued terrestrial data and the cross-over adjusted airborne estimates

Lines	F-2017 with TC (mGal)			F-2018 with iTempStab (mGal)		
	μ	σ	RMSE	μ	σ	RMSE
L1	2.71	2.27	2.50	− 1.37	1.67	1.66
L2	0.08	3.41	2.41	0.06	1.22	1.69
L3	− 1.97	1.49	1.75	− 1.03	1.05	1.21
L4	− 2.09	2.53	2.32	− 1.29	0.84	1.24
L5	− 2.67	1.53	2.17	− 2.13	0.64	1.36
L6	− 1.83	2.81	2.37	− 0.11	0.87	1.97
L7	− 3.24	1.93	2.66	− 2.11	0.98	1.30
L8	− 1.53	1.48	1.51	− 2.96	0.72	1.85
L9	2.71	2.27	2.50	1.40	0.51	1.05
Mean	− 0.87	2.19	2.24	− 1.06	0.94	1.48

TC temperature correction, μ mean, σ standard deviation, *RMSE* RMS/$\sqrt{2}$

satellite-only global gravity model (Kvas et al. 2019) up to degree and order 220 and residual terrain modeling effects (Forsberg 1984) computed from 7.2″ resolution SRTM data constructed by Hirt et al. (2014) were removed from the terrestrial free-air gravity anomalies. Subsequently, a covariance function was estimated and fitted to the residual free-air gravity anomaly data using the GRAVSOFT suite of programs (Forsberg and Tscherning 2008). Finally, the removed global model and RTM effects were restored to obtain the final upward continued gravity disturbance values.

Figure 8 shows the spatial differences between the cross-over adjusted vertical gravity disturbances and the upward continued data for both flights. In Fig. 9, along-track comparisons of the upward continued terrestrial gravity values with the cross-over adjusted airborne gravity estimates at two sample lines (Line-3 and Line-8, see Fig. 2a) are displayed. The statistics of the residuals for all lines are given in Table 4. While the maximum deviations occur at the starts and ends of the lines which are close to the aircraft turns, the agreement or correlations between two data series are quite strong at the remaining parts. The F-2018 residuals are in the range of ± 5 mGal in most of the survey area, but they could reach up to ± 10 mGal in F-2017. The variability of the F-2018 flight residuals is almost constant throughout the region and 57% less than that of the F-2017 flight. The F-2018 flight with iTempStab produced also better RMSE statistics than F-2017. While the maximum RMSE of the F-2018 is about 1.9 mGal and the mean of all lines is about 1.5 mGal, these statistics increase at least 30% in the case of F-2017.

5 Conclusion

The performance of a thermal stabilization system named iTempStab recently produced by iMAR Navigation GmbH was tested in central Turkey. The internal and external quality assessment of vertical gravity disturbance estimates of the two test flights was evaluated at the cross-over points and also comparisons were performed with upward continued ground data.

The RMSE of the non-adjusted cross-over differences were reduced by 50% from 2.6 to 1.3 mGal, and the constant-bias was avoided with the contribution of iTempStab. Applying an adjustment to the network of cross-overs leads to significantly smaller residuals. The adjusted cross-over residuals of the F-2018 flight have RMSE of about 0.5 mGal, which is a highly satisfactory precision for the strapdown gravimetry.

The comparison with upward continued ground gravity data at flight altitudes suggests that the thermal stabilization system yields better residual statistics in terms of residual range, variability, and RMSE. While the range of the residuals is about ± 10 mGal in F-2017, it reduces to ± 5 mGal in F-2018. With the contribution of the iTempStab, the mean of the standard deviation of the residuals is reduced from 2.19 to 0.94 mGal, and the RMSE is reduced from 2.24 to 1.48 mGal, respectively. The findings of the study suggest that the thermal stabilization system significantly improves the accelerometer stability and thus the precision and accuracy of the strapdown airborne gravity estimates.

Author contributions All the authors contributed to the design of the study and came up with the idea of the research. MS processed the SIMU and GNSS data with the help of DB. HY performed upward continuation of terrestrial gravity data. MH is the project manager of iTempStab. MS drafted the manuscript. All authors read and approved the final manuscript.

References

Ayres-Sampaio D, Deurloo R, Bos M, Magalhães A, Bastos L (2015) A comparison between three IMUs for strapdown airborne gravimetry. Surv Geophys 36(4):571–586. https://doi.org/10.1007/s10712-015-9323-5

Becker D (2016) Advanced calibration methods for strapdown airborne gravimetry. Ph.D. Thesis, Technische Universität Darmstadt, Darmstadt, Germany. https://tuprints.ulb.tu-darmstadt.de/5691/. Accessed 28 Oct 2019

Becker D, Nielsen JE, Ayres-Sampaio D, Forsberg R, Becker M, Bastos L (2015) Drift reduction in strapdown airborne gravimetry using a simple thermal correction. J Geod 89:1133–1144. https://doi.org/10.1007/s00190-015-0839-8

Bruton AM, Schwarz KP, Ferguson S, Kern M, Wei M (2002) Deriving acceleration from DGPS: toward higher resolution applications of airborne gravimetry. GPS Solut 5(3):1–14. https://doi.org/10.1007/PL00012894

Deurloo RA (2011) Development of a Kalman filter integrating system and measurement models for a low-cost strapdown airborne gravimetry system. Ph.D. Thesis, Faculty of Sciences, University of Porto, Porto, Portugal

Deurloo R, Yan W, Bos M, Ayres-Sampaio D, Magalhães A, Becker M, Becker D, Bastos L (2015) A comparison of the performance of medium-and high-quality inertial systems grades for strapdown airborne gravimetry. In: Rizos C, Willis P (eds) IAG 150 years. International association of geodesy symposia, vol 143. Springer, Cham, pp 323–329. https://doi.org/10.1007/1345_2015_18

Forsberg R (1984) A study of terrain reductions, density anomalies and geophysical inversion methods in gravity field modeling. Report no. 355, Department of Geodetic Science and Surveying, The Ohio State University, Columbus, USA. https://earthsciences.osu.edu/geodetic/resources/osu-reports. Accessed 28 Oct 2019

Forsberg R, Olesen AV (2010) Airborne gravity field determination. In: Xu G (eds) Sciences of geodesy-I. Springer, Berlin Heidelberg, pp 83–104. https://doi.org/10.1007/978-3-642-11741-1_3

Forsberg R., Tscherning CC (2008) An overview manual for the GRAVSOFT geodetic gravity field modelling programs. Technical Report, Danish Space Center, Technical University of Denmark, Lyngby, Denmark

Forsberg R, Olesen AV, Keller K, Møller M, Gidskehaug A, Solheim D (2001) Airborne gravity and geoid surveys in the Arctic and Baltic Seas. In: Proceedings of international symposium on kinematic systems in geodesy, Geomatics and Navigation (KIS-2001), Banff, pp 586–593

Gelb A (1974) Applied optimal estimation. The M.I.T Press, Cambridge. ISBN 0-262-20027-9

Glennie C, Schwarz KP (1999) A comparison and analysis of airborne gravimetry results from two strapdown inertial/DGPS systems. J Geod 73(6):311–321. https://doi.org/10.1007/s001900050248

Glennie CL, Schwarz KP, Bruton AM, Forsberg R, Olesen AV, Keller K (2000) A comparison of stable platform and strapdown airborne gravity. J Geod 74(5):383–389. https://doi.org/10.1007/s001900000082

Groves PD (2013) Principles of GNSS, inertial, and multisensor integrated navigation systems, 2nd edn. Artech House, Boston, MA, USA, London, UK. ISBN 978-1-60807-005-3

Heiskanen WA, Moritz H (1967) Physical geodesy. WH Freeman and Company, San Francisco, CA, USA

Hirt C, Kuhn M, Claessens S, Pail R, Seitz K, Gruber T (2014) Study of the earth's short-scale gravity field using the ERTM2160 gravity model. Comput Geosci 73:71–80. https://doi.org/10.1016/j.cageo.2014.09.001

Hwang C, Hsiao Y-S, Shih H-C (2006) Data reduction in scalar airborne gravimetry: theory, software and case study in Taiwan. Comput Geosci 32(10):1573–1584. https://doi.org/10.1016/j.cageo.2006.02.015

Jekeli C (1994) Airborne vector gravimetry using precise, position-aided inertial measurement units. Bulletin géodésique 69(1):1–11. https://doi.org/10.1007/BF00807986

Jekeli C, Kwon JH (1999) Results of airborne vector (3-d) gravimetry. Geophys Res Lett 26(23):3533–3536. https://doi.org/10.1029/1999GL010830

Jensen TE (2018) Airborne strapdown gravity measurements for geodesy and geophysics. Ph.D. Thesis, Kgs. Lyngby: Technical University of Denmark. https://orbit.dtu.dk/ws/files/164587031/Main.pdf. Accessed 28 Oct 2019

Jensen TE, Forsberg R (2018) Helicopter test of a strapdown airborne gravimetry system. Sensors 18(9):3121. https://doi.org/10.3390/s18093121

Jensen TE, Olesen AV, Forsberg R, Olsson PA, Josefsson Ö (2019) New results from strapdown airborne gravimetry using temperature stabilisation. Remote Sens 11(22):2682. https://doi.org/10.3390/rs11222682

Kaas E, Sørensen B, Tscherning CC, Veicherts M (2013) Multiprocessing least squares collocation: applications to gravity field analysis. J Geod Sci 3(3):219–223. https://doi.org/10.2478/jogs-2013-0025

Kvas A, Mayer-Gürr T, Krauss S, Brockmann JM, Schubert T, Schuh W-D, Pail R, Gruber T, Jäggi A, Meyer U (2019) The satellite-only gravity field model GOCO06s. Paper presented at EGU General Assembly 2019, Vienna, Austria. 10.13140/RG.2.2.14101.99047

Kwon JH, Jekeli C (2001) A new approach for airborne vector gravimetry using GPS/INS. J Geod 74(10):690–700. https://doi.org/10.1007/s001900000130

Moritz H (2000) Geodetic reference system 1980. J Geod 74(1):128–133. https://doi.org/10.1007/s001900050278

Rauch HE, Striebel CT, Tung F (1965) Maximum likelihood estimates of linear dynamic systems. AIAA J 3(8):1445–1450. https://doi.org/10.2514/3.3166

Sampietro D, Capponi M, Mans AH, Gatti A, Marchetti P, Sansò F (2017) Space-Wise approach for airborne gravity data modelling. J Geod 91:535–545. https://doi.org/10.1007/s00190-016-0981-y

Schwarz KP, Wei M (1990) A framework for modelling kinematic measurements in gravity field applications. J Geod 64(4):331–346. https://doi.org/10.1007/BF02538407

Schwarz KP, Colombo O, Hein G, Knickmeyer ET (1992) Requirements for airborne vector gravimetry. In: Colombo OL (eds) From mars to greenland: charting gravity with space and airborne instruments. International Association of Geodesy Symposia, vol 110. Springer, New York, NY. https://doi.org/10.1007/978-1-4613-9255-2_25

Simav M, Yildiz H (2019) Evaluation of EGM2008 and latest GOCE-based satellite only global gravity field models using densified gravity network: a case study in south-western Turkey. Bollettino di Geofisica Teorica ed Applicata 60(1):49–68. https://doi.org/10.4430/bgta0255

Tomé P (2002) Integration of inertial and satellite navigation systems for aircraft attitude determination. Ph.D. dissertation, Faculty of Sciences, University of Porto, Porto, Portugal

Wei M, Schwarz KP (1998) Flight test results from a strapdown airborne gravity system. J Geod 72(6):323–332. https://doi.org/10.1007/s001900050171